Vacuum 238 (2025) 114254

Contents lists available at ScienceDirect

Vacuum

journal homepage: www.elsevier.com/locate/vacuum

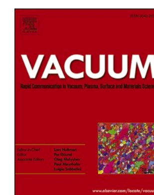

Thermal and plasma-enhanced ALD for the synthesis of inverse opal Al_2O_3 and its composite materials

Hamsasew Hankebo Lemago [a,e,*], Soeun Choi Arwen [a], Dóra Hessz [c,d], Gyula Jágerszki [a], Petra Pál [b], Csaba Cserháti [b], Eszter Mónika Baradács [b,f], Tamás Fodor [g], Zoltán Erdélyi [b], Imre Miklós Szilágyi [a,**]

[a] Department of Inorganic and Analytical Chemistry, Faculty of Chemical Technology and Biotechnology, Budapest University of Technology and Economics, Műegyetem rkp. 3, H-1111, Budapest, Hungary
[b] Department of Solid-State Physics, Faculty of Sciences and Technology, University of Debrecen, P.O. Box 400, 4002, Debrecen, Hungary
[c] Department of Physical Chemistry and Materials Science, Faculty of Chemical and Bioengineering, Budapest University of Technology and Economics, Műegyetem rkp. 3, H-1111, Budapest, Hungary
[d] Institute of Materials and Environmental Chemistry, Research Centre for Natural Sciences, HUN-REN Research Network, P.O. Box 286, Budapest, H-1519, Hungary
[e] Department of Chemistry, College of Natural and Computational Science, Wachemo University, Hossana, 667, Ethiopia
[f] Department of Environmental Physics, Faculty of Sciences and Technology, University of Debrecen, P.O. Box 400, 4002, Debrecen, Hungary
[g] HUN-REN Institute for Nuclear Research, H-4002, Debrecen, Hungary

ARTICLE INFO

Handling Editor: Prof. L.G. Hultman

Keywords:
Al_2O_3 inverse opal
Thermal ALD
Plasma-enhanced ALD
Al_2O_3/ZnO composite
Al_2O_3/TiO_2composite

ABSTRACT

This study explores the synthesis and characterization of inverse opal photonic crystals (IOPC) composed of Al_2O_3 and its composites, coated with ultra-thin ZnO and TiO_2 layers using thermal atomic layer deposition (TALD) and plasma-enhanced ALD (PEALD). Polystyrene (PS) opal nanospheres (460 nm) served as a template on a silicon wafer. Al_2O_3 was infiltrated into a PS opal template and subsequently calcined to remove the template. Ultra-thin ZnO and TiO_2 layers were deposited via TALD/PEALD to form composite IOPCs. Characterization by SEM/EDX, TG, UV–Vis spectroscopy, atomic force microscopy (AFM), photoluminescence (PL), and XPS confirmed the periodic, interconnected IO structures. The Al_2O_3 IOPC demonstrated template removal and a reduced sphere diameter to ~433 nm. Composite structures-maintained periodicity, with TALD yielding smoother surfaces compared to PEALD. The incorporation of ZnO and TiO_2 layers increased surface roughness. UV–Vis spectroscopy revealed absorption peaks at 275 nm for Al_2O_3, with additional peaks at 400 nm and 529 nm related to the photonic band gap and slow photon effects. XPS analysis reveals characteristic peaks for Al_2O_3, ZnO, and TiO_2, along with oxygen vacancies and aluminum hydroxide formation, while elemental data highlight successful ZnO and TiO_2 incorporation with PEALD outperforming TALD in ZnO deposition. In this study PEALD enhanced film growth and tailored properties, while TALD offered smooth, conformal coatings and precise control over IOPC properties, both contributing to the design of advanced IO-based photonic materials.

1. Introduction

Inverse opal photonic crystals (IOPC) are captivating nanomaterials with a 3D network of interconnected air voids arranged in a super-ordered, periodic pattern. Unlike natural opals that play with light due to density variations, IOPC manipulates light through this unique architecture. The periodicity acts like a natural photonic filter, a photonic bandgap (PBG), that selectively allows certain light wavelengths to pass through while reflecting others. By precisely controlling the size, arrangement, and material used for the pores, researchers can tailor this PBG to achieve specific functions. This allows IOPC to be designed for various applications, from efficient light sources and waveguides to highly sensitive light detectors, propelling them to the forefront of advanced material research [1–3].

Nanolithography and the self-assembly of colloidal microspheres are two prevalent techniques employed in fabricating inverse opal (IO)

* Corresponding author. Department of Inorganic and Analytical Chemistry, Faculty of Chemical Technology and Biotechnology, Budapest University of Technology and Economics, Műegyetem rkp. 3, H-1111, Budapest, Hungary.
** Corresponding author.
E-mail addresses: hamsasew.lemago@edu.bme.hu (H.H. Lemago), szilagyi.imre.miklos@vbk.bme.hu (I.M. Szilágyi).

https://doi.org/10.1016/j.vacuum.2025.114254
Received 13 August 2024; Received in revised form 10 March 2025; Accepted 11 March 2025
Available online 12 March 2025
0042-207X/© 2025 The Authors. Published by Elsevier Ltd. This is an open access article under the CC BY license (http://creativecommons.org/licenses/by/4.0/).

structures. Nanolithography, referred to as the "top-down" approach, is relatively expensive and time-consuming, resulting in the formation of only a few structural layers of materials. On the other hand, the "bottom-up" method, involving the self-assembly of colloidal microspheres, offers a cost-effective means to prepare crystalline samples comprising even up to several hundred structural layers of thickness [3–5]. In the bottom-up approach, various templates such as SiO_2, PS, or polymethyl methacrylate (PMMA) spheres are meticulously arranged into opal photonic crystal (PC) using methods like gravity sedimentation, centrifugal sedimentation, self-assembly, evaporation, dip coating, or electrophoresis. These opal PCs then serve as the templates into which the desired precursor or target material is introduced. Subsequently, the template is removed either through calcination or etching, resulting in the formation of the IOPC. Throughout the preparation process, different methods can be employed to fill the precursor or target material, including chemical vapor deposition, ALD, electrochemical deposition, sol-gel method, and more [5–7].

Atomic layer deposition (ALD) presents a promising and innovative synthetic pathway for creating IOs due to its exceptional step coverage, conformality, and ability to grow dense films with precise control over atomic structures. It is a deposition technique used to produce thin films with utmost precision at the atomic scale by sequentially depositing individual atomic layers through self-limiting surface gas-solid reactions. This process takes place under specific pressure and temperature conditions, facilitating controlled material deposition onto a substrate. A suitable vacuum environment within the ALD system ensures the precise delivery and reaction of precursor gases, enabling efficient by-product removal and preventing contamination. This controlled environment is critical for achieving clean growth surfaces, optimizing reaction kinetics, and ensuring the conformality and quality of the deposited films. Typically, the substrate is housed in a separate compartment connected to the reactor. To produce IO nanostructures through ALD, the initial step involves the self-assembly of polymer templates on conventional substrates like glass, metal sheets, or silicon wafers, forming colloid crystals. Precursors, consisting of metal and oxidants, are introduced into the ALD reactor sequentially using N_2 or Ar gas. The infiltrated opal undergoes high-temperature treatment in the presence of air to transform into ALD metal oxide IOs, decomposing and evaporating the polymer opal layer, leaving behind the desired metal oxide IO structure [8–13].

Furthermore, there are two main ALD process modes: Thermal ALD (TALD) and plasma-enhanced ALD (PEALD). TALD relies on surface reactions for film growth. This allows for excellent control over thickness and conformality but often requires higher temperatures (150–350 °C). This can be crucial for IOs with temperature-sensitive templates that might degrade at higher temperatures used in TALD. PEALD utilizes a precursor in the plasma state to improve reaction rates and broaden precursor compatibility. This allows for lower deposition temperatures and enables film growth on heat-sensitive materials. PEALD often exhibits faster growth rates compared to TALD due to the additional energy provided by the plasma. However, while PEALD can achieve higher film purity and growth rates, this faster growth can sometimes lead to less conformal film growth, which is undesirable for complex structures like IOs where good coverage of the pores is essential, and it can introduce challenges like non-conformal coverage on high aspect ratio features and complex reactor designs [14–16].

This study aims to investigate the influence of ALD techniques on the structural, compositional, optical, and photoluminescent properties of Al_2O_3-based IOPCs and their composites with TiO_2 and ZnO. We used PS 460 nm opal nanospheres as a sacrificial template material, which was deposited on the surface of a Si wafer substrate. In the interstitial voids, 36 nm thick Al_2O_3 was infiltrated using TALD techniques, followed by calcination at a higher temperature to remove the opal and produce a hollow Al_2O_3 IO macrostructure. Before removing the template, an ultrathin layer of ZnO or TiO_2 was coated on the surface of the pristine Al_2O_3 using either TALD or PEALD techniques to produce Al_2O_3/ZnO or Al_2O_3/TiO_2 composites, respectively. Our research group successfully synthesized various types of IO structures and their composites, including TiO_2/Al_2O_3, ZnO/Al_2O_3, and TiO_2/ZnO IO composites, using both ALD techniques [17–19]. Studies have shown that an ultrathin Al_2O_3 layer, coated on TiO_2 or ZnO IO structures synthesized using both TALD and PEALD techniques, exhibited promising photocatalytic properties while minimizing the impact on the crystal structure of the IO materials.

2. Experimental procedure

2.1. Opal template preparation

The PS opal template (Sigma Aldrich) was fabricated using a Si wafer and commercially purchased PS nanospheres with an average diameter of ~460 nm. First, a 0.15 ml suspension of 0.3 wt % PS nanospheres was diluted with 4.85 ml of deionized water in a glass container. The container was immediately sealed to prevent evaporation. Gentle manual stirring was followed by a 2-h ultrasonication process at 40 °C to disperse and aggregate the PS nanospheres. A Si wafer (planar substrate) was prepared concurrently. After cutting it to a size of 2.5*2.5 cm, it underwent a cleaning process to remove contaminants. The cleaning involved washing with soap to eliminate organic residues from handling or storage, followed by ethanol treatment to remove both organic and inorganic impurities. Finally, the Si wafer was rinsed thoroughly with ion exchange water to ensure the complete removal of any remaining contaminants.

Following the cleaning procedure, the substrate was immersed in a so-called piranha solution (3:1H_2SO_4:H_2O_2) for at least 2 h under a fume hood. This step aimed to remove impurities and improve the hydrophilicity of the substrate. The piranha solution was prepared by mixing 30 ml of H_2SO_4 with 10 ml of H_2O_2. After ultrasonication, the Si substrate was tilted at a 45-degree angle and placed into the PS suspension. This facilitated the vertical deposition and self-assembly of the colloidal particles onto the substrate. The entire assembly was then placed in a furnace for colloidal crystal formation through solvent evaporation and self-assembly. The heating program involved a gradual temperature increase: from room temperature to 50 °C over 1.5 h, followed by a holding time of 14 h at 50 °C. Finally, the temperature was raised to 80 °C for another 1.5 h to complete solvent evaporation.

2.2. Atomic layer deposition techniques: TALD vs PEALD

Before initiating ALD using the Beneq TFS-200-186 system, the ALD chamber was preheated to 45–50 °C for 2 h in preparation for the thermal mode ALD process. Subsequently, the samples and a reference Si wafer [(100)] were simultaneously placed into the ALD reactor to begin the film growth process. In this process, N_2 (99.999 %) served as the carrier gas, maintaining a pressure of 6.8 mbar within the vacuum chamber and 1.4 mbar within the reactor. During the PEALD deposition, a constant RF power of 50 W was applied to the plasma to activate the O_2 oxidant. Internal pressures of 7.4 mbar and 1.2 mbar were maintained within the vacuum chamber and deposition reactor, respectively. The pulse and purge sequence for either TALD or PEALD is given in the table below.

For Al_2O_3, ZnO, and TiO_2 the ALD precursors were trimethylaluminum (TMA), diethylzinc (DEZ), and titanium tetrachloride ($TiCl_4$) respectively, along with ultra-pure water as a common reactant for all three processes.

Moreover, the vacuum system of the ALD chamber was maintained at a constant pressure of 6.8 mbar (N_2) during TALD and 7.4 mbar (Ar) during PEALD. This controlled vacuum environment ensured optimal precursor delivery and reaction kinetics, leading to the precise deposition of high-quality thin films. The vacuum system also facilitated the efficient removal of by-products and excess reactants, preventing contamination and ensuring clean growth surfaces.

2.3. Annealing program

The Al_2O_3 IO samples were subjected to an annealing process following a predefined heating program. This heat treatment procedure aimed to eliminate the sacrificial template material by placing both the samples and control samples within alumina ceramic crucibles. The annealing program was chosen considering TG analysis for effectiveness. The entire process was carried out in a furnace (Nabertherm L9/11/B410, Germany) under ambient air conditions. The heating program involved a stepwise temperature increase. Initially, the samples were heated from room temperature to 500 °C over 4 h. This was followed by maintaining the temperature at 500 °C for an additional half-hour. During this stage, the PS nanospheres which served as the template material, were effectively removed. Subsequently, the temperature was gradually raised to 900 °C for 1 h. Once the temperature reached 900 °C, it was held constant for 2 h. This final step ensured the complete removal of any residual template material and promoted the desired structural transformations within the Al_2O_3 IO samples.

2.4. Characterization

Thermogravimetry (TG) analysis of the PS was conducted using a TA Instruments SDT 2960 device in an air and N_2 atmosphere to determine suitable annealing temperatures for PS template and ALD process conditions. The heating rate of 2 °C/min was applied up to 600 °C. The PS sample film was collected in Pt crucibles after being scratched off from the glass surface.

The morphology was examined with SCIOS™ 2 DualBeam™ FIB-SEM (Thermo Fisher Scientific) equipped with an in-lens secondary electron detector and a field emission gun source, which featured unique electron optical components, including the annular in-column detector system. The surface analysis occurred within a low-voltage system where an acceleration voltage of 1 kV and an electron current of 10 pA. To counteract the charging effect on uncoated samples, a reverse bias of 20 V was applied to the specimen holder.

EDX spectra were captured using the JEOL JSM-5500LV SEM, with three measurement points taken for each sample and then they were averaged.

The surface roughness and morphology of the samples were characterized using atomic force microscopy (AFM) with a Nanosurf C3000 controller. The AFM images and root mean square (RMS) values were obtained and analyzed using Gwyddion version 2.64 software.

The photonic bandgap (PBG) of the Al_2O_3 and composite IO materials has been estimated by using a modified Bragg's equation (2), shown below:

$$\lambda_{max} = 1.632D\left(n_{avg}^2 - \mathrm{Sin}^2\,\theta\right)^{1}/^{2} \quad (1)$$

Where λ_{max} is the wavelength of the photonic band maximum of the materials, D is the diameter of spheres (would generally be taken as 2r, where r is the sphere radius.), θ is the angle between the incident light and the surface of the sample ($\theta = 0°$). The average refractive index n_{avg} of the samples can be calculated using the following equations (2) and (3) [20]:

For pure Al_2O_3 IO and composites (eg. Al_2O_3/ZnO) the n_{avg}, can be calculated as;

$$n_{avg} = n_{Al2O3} f_{Al2O3} - \left(1 - f_{Al2O3}\right) n_{air} \quad (2)$$

$$n_{avg} = f_{ZnO} n_{ZnO+} f_{Al2O3} n_{Al2O3} - \left(1 - f_{ZnO} - f_{Al2O3}\right) n \quad (3)$$

Where f is the filling factor of the solid sphere. In face-centered cubic structures, spheres occupy about 74 % of the space, with the remaining 26 % residing between specific lattice planes. When alternating layers of TiO_2 and ZnO are deposited, their combined filling factor can be calculated, but adjustments are needed to maintain the total void fraction of 26 %. $n_{PS} = 1.6$, $n_{Al2O3} = 1.8$, $n_{TiO2} = 2.5$, $n_{ZnO} = 2.0$ and $n_{air} =$ 1.0 are the refractive indices of PS, Al_2O_3, TiO_2, ZnO, and air, respectively.

UV–Vis spectroscopy of samples was recorded with a UV–Visible spectrometer Avantes AvaSpec-2048 fiber optic spectrometer with an Ava-Light–DHS light source applying AvaSoft software in reflectance mode.

Spectroscopic ellipsometry (Semilab SE-2000) was used to determine the film thickness of the reference samples. For this, reference Si (100) wafers were also introduced as control samples into the ALD system together with the opal and IO samples.

Photoluminescence (PL) spectra were recorded using an Edinburgh Instruments FS5 spectrofluorometer with a stationary fluorescence setup, featuring an excitation wavelength of 320 nm at room temperature and the inclusion of a long pass glass filter in the emission beam set at a nominal wavelength of 320 nm.

The X-ray photoelectron spectroscopy (XPS) measurements were conducted using an XR 50 dual-anode, non-monochromatized X-ray source and a Phoibos 100 MCD-5 hemispherical energy analyzer by SPECS (Berlin, Germany). Samples were mounted onto copper sample holders using double-sided adhesive tape and degassed in the high vacuum of the sample loading chamber ($\sim 10^{-7}$ mbar) overnight before being transferred into the spectrometer. The base vacuum of the instrument was maintained at 5×10^{-10} mbar. During the measurements, samples were cooled with liquid nitrogen, and the pressure remained below 10^{-8} mbar. Spectra were acquired sequentially using Al K_α radiation (1486.6 eV) with an acceleration voltage of 10 kV and an emission current of 10 mA (100 W X-ray power). The binding energy scale was calibrated using the Au 4f and Cu 2p peaks of a freshly cleaned reference sample containing both metals, as per the manufacturer's instructions. Charge referencing was performed using the C 1s peak of carbon (284.8 eV) which is rightfully considered untrustworthy, as detailed in Ref. [21] and some other works from these authors, however in our case the spectra were mainly used for confirming the elemental composition in the samples, which does not require truly rigorous charge correction. Data processing was carried out using CasaXPS software.

3. Result and discussion

Fig. 1 outlines the fabrication process for Al_2O_3 IO macrostructures and their composites. A sacrificial template of 460 nm PS is deposited on a high thermal stability Si wafer using vertical deposition (step 1). TALD infiltrates Al_2O_3 into the template's void spaces, followed by high-temperature removal of the PS template to achieve the final Al_2O_3 IO (steps 2 and 3). The structure undergoes annealing and high-temperature treatment for further consolidation. For composite materials, an additional 5 nm hybrid layer is grown using either TALD or PEALD before template removal and high-temperature crystallization (steps 3 and 4). Finally, TALD and PEALD are used to deposit Al_2O_3/ZnO and Al_2O_3/TiO_2, respectively.

3.1. Thermal analysis of template both in air and N_2 environments

The PS-460 template showed minimal mass loss (0.6 % in N_2, 0.3 % in air) up to 200 °C (Fig. 2a and b). Thermal analysis revealed two decomposition stages under both N_2 and air environments. The first stage (polymer decomposition) resulted in a smaller mass loss (91.2 % remaining mass in N_2, 95.5 % in air) between 265 and 380 °C (N_2) or 280–390 °C (air) (See Fig. 2a). The second stage (char decomposition) showed the main mass loss step (7.0 % remaining mass in N_2, 1.7 % in air) between 380 and 600 °C (N_2) or 390–600 °C (air in Fig. 2b). Based on this, annealing at 500 °C in N_2 is sufficient for template removal and is compatible with TALD and PEALD processes.

3.2. Morphological analysis by SEM

SEM analysis (Fig. 3a) confirmed the successful synthesis of opal

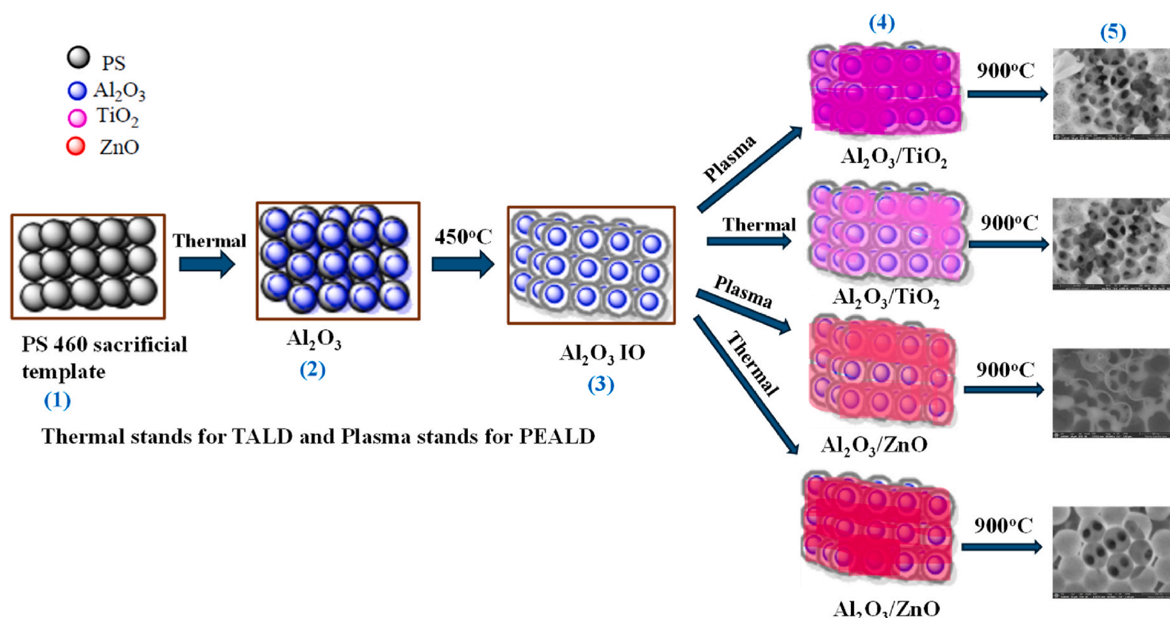

Fig. 1. The fabrication process for Al_2O_3 IOs and their composites: (1) PS template synthesis (VLD), (2) Al_2O_3 infiltration via TALD, (3) template removal and Al_2O_3 IO formation, (4) optional hybrid layer growth (TALD or PEALD), (5) final crystallization by higher temperature.

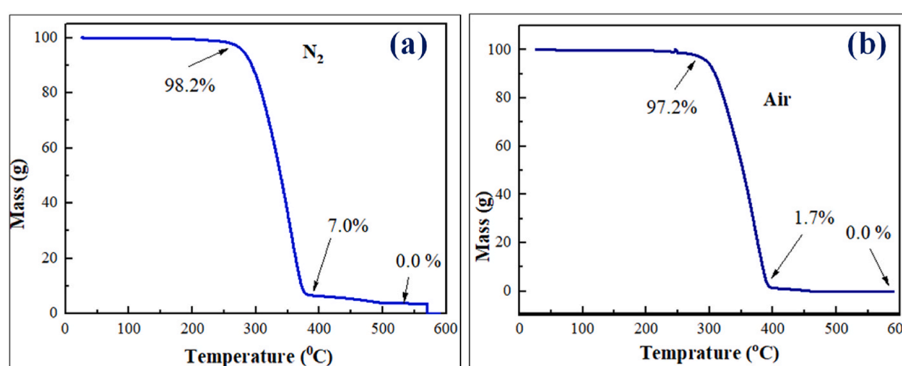

Fig. 2. TG measurement of PS nanosphere template in N_2 (a) and air (b) environment.

structures from ~460 nm PS nanospheres. These structures exhibited an interconnected network of IO structures with periodic arrays and uniform pore sizes. The PS nanosphere template itself displayed uniform and compact pores arranged in a hexagonal pattern [22], a tightly packed structure where spheres are arranged like a honeycomb. For the pure Al_2O_3 IO, SEM revealed successful infiltration of the opal voids with Al_2O_3 using ALD (Fig. 3b and c). High-temperature annealing removed the opal template, forming the final IO structure. However, this process induced cracks and a slight shrinkage in sphere size, as observed in the SEM images. Direct SEM measurements placed the sphere diameter at ~433 nm and material thickness at ~39 nm. Ellipsometry, another measurement technique, suggested a slightly thinner thickness of ~36 nm. The final IO structure possessed a face-centered cubic (FCC) arrangement, where spheres are positioned at the corners and centers of a cube [23].

Furthermore, additional cross-sectional views of the IO samples are presented in Fig. S3. We successfully deposited an ultra-thin (~5 nm) overlayer on top of the pure Al_2O_3 templates using combined TALD and PEALD infiltration techniques. These composite structures retained an interconnected and periodic arrangement of spheres inherited from the original PS nanosphere template. The two deposition methods resulted in slightly different thicknesses and void sizes. TALD infiltration (Al_2O_3/ZnO and Al_2O_3/TiO_2) made minimal changes to the overall thickness material. Based on the SEM analysis, the average TALD composite layer thickness was approximately 41 nm for composite Al_2O_3/ZnO and Al_2O_3/TiO_2, respectively, with a void diameter of 429 nm (See Fig. 3d–g).

In contrast to TALD, PEALD (Fig. 3h–k) induced slightly larger changes. The void size decreased to 415 nm, while the composite layer thickened to 47 nm and 48 nm for Al_2O_3/ZnO and Al_2O_3/TiO_2 composites, respectively. Despite the increase in thickness, the double-layered spheres retained their spherical shape. These observations suggest that TALD provides smoother surfaces and better conformality compared to PEALD. This is likely due to PEALD's plasma activation step, which can roughen surfaces and reduce the ability of the film to coat complex geometries (conformality). While PEALD offers lower deposition temperatures, the resulting films may be microscopically rough and deviate from the ideal atomic composition (stoichiometry). Additionally, bulky PEALD precursors have difficulty penetrating deep into highly porous substrates, leading to non-uniform film growth within the pores [24,25] (see Table 1).

3.3. Compositional analysis by EDX

Table 2 and Fig. S1 provide a detailed overview of the elemental composition of six ALD samples produced using two different

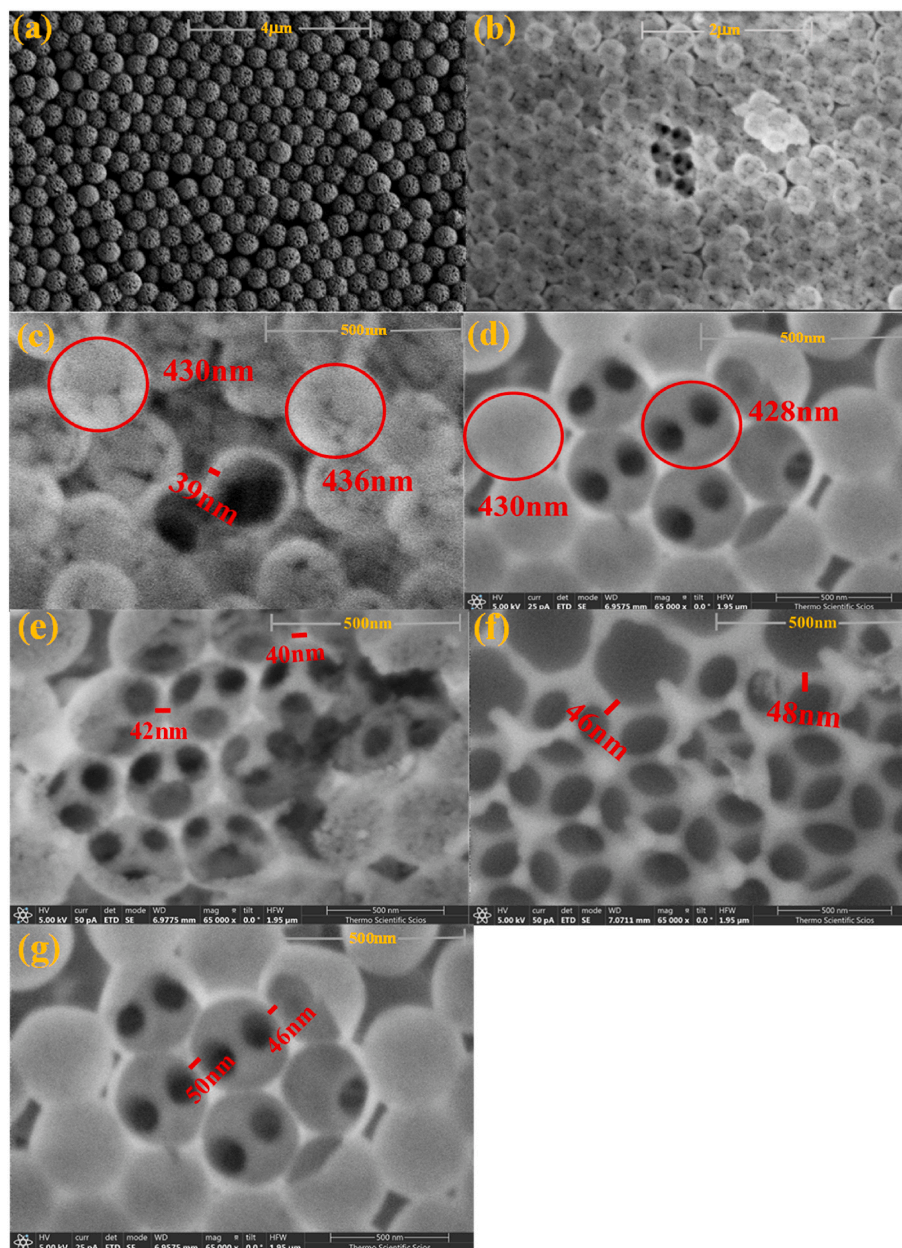

Fig. 3. SEM pictures of (a) PS nanosphere template, (b–c) pure Al_2O_3 IO, (d) TALD Al_2O_3/ZnO, (e) TALD Al_2O_3/TiO_2, (f) PEALD Al_2O_3/ZnO, and (g) PEALD Al_2O_3/TiO_2 respectively.

techniques: a combination of TALD and PEALD. These samples underwent high-temperature annealing, reaching up to 900 °C. As a result, no detectable carbon content was found, confirming the efficiency of the annealing process in eliminating any organic template material. The primary elements identified in the samples are Aluminum (Al), Oxygen (O), Titanium (Ti), and Zinc (Zn), which suggest the presence of Al_2O_3, TiO_2, and ZnO. Additionally, trace amounts of Silicon (Si) were detected, likely originating from the silicon wafer substrate. The absence of organic carbon in all samples highlights the thoroughness of the annealing process.

3.4. Surface roughness analysis by atomic force microscopy

Atomic Force Microscopy (AFM) emerged as a powerful tool for characterizing surface topography at the nanoscale. It thoroughly scans a sharp probe across the specimen surface, measuring the minute forces between them. These interactions translate into a detailed topographic map, revealing surface features like height variations, roughness, and overall morphology [26]. AFM was utilized in this study to characterize the surface roughness of IO structures fabricated with Al_2O_3 using ALD. Fig. 4 shows a periodically ordered close-packed structure that exhibits a triangular arrangement characteristic of plane 111 within a fcc system [27]. The investigation further explored the effects of incorporating ZnO and TiO_2 layers into the IO structure. The study focused on roughness: RMS (Root Mean Square), commonly used to quantify surface texture. The results revealed a surface roughness dependence on material composition and deposition methods within the composite structures.

The study investigated the influence of deposition methods on the surface roughness of composite structures. In Fig. 5, straighter lines correspond to smoother surfaces, whereas more jagged or uneven lines indicate rougher surfaces. As observed in Fig. 4 a&b, pristine Al_2O_3 IO (13.8 nm RMS) exhibited a smoother surface compared to the sacrificial PS opal template (20.3 nm RMS). However, the RMS spectrum in Fig. 4 reveals less jagged lines for the composite materials. The incorporation

Table 1
ALD preparation program.[a].

Samples	ALD Mode	Thickness (nm)	ALD cycle	GPC (nm)	Temp (^{0}C)	Pulse/Purge Steps
Al_2O_3 IO	Thermal	36	133	0.27	50	0.15s TMA, 0.5s N_2, 0.15s H_2O, and 0.75s N_2
Al_2O_3/ ZnO-T	Thermal	5	55	0.09	50	0.1s DEZ pulse, 1.5s N_2 purge, 0.15s H_2O pulse, and 1.5s N_2 purge
Al_2O_3/ ZnO-P	Plasma	5	37	0.13	50	0.15s DEZ, 2s Ar purge, 2s O_2 (plasma), 2s Ar purge
Al_2O_3/ TiO_2-T	Thermal	5	52	0.09	50	0.3s $TiCl_4$, 3s Ar, 0.3s H_2O, 3s N_2
Al_2O_3/ TiO_2-P	Plasma	5	48	0.10	50	0.15s $TiCl_4$, 2s Ar purge, 2s O_2 (plasma), 2s Ar purge

[a] GPC stands for growth per cycle, DEZ stands for diethyl zinc, and TMA stands for trimethyl aluminum.

Table 2
EDX Compositional analysis of the samples.

Samples Name	Element (At. Wt %)					
	C	O	Al	Ti	Zn	Si
PS-460 nm	87.0	3.0	–	–	–	10.0
Al_2O_3 IO	–	50.8	41.2	–	–	8.0
Al_2O_3/ZnO-T	–		27.4	–	5.5	7.0
Al_2O_3/ZnO-P	–	58.6	38.0	–	8.4	9.0
Al_2O_3/TiO_2-T	–	47.2	35.2	6.6	–	11.0
Al_2O_3/TiO_2-P	–	47.6	33.3	9.1	–	10.0

of ZnO or TiO_2 layers using either TALD or PEALD methods into the IO structure resulted in a noticeable increase in surface roughness. For ZnO/Al_2O_3 composites, thermally deposited using ALD (17 nm RMS) yielded slightly smoother surfaces compared to those achieved using plasma ALD (19 nm RMS). As illustrated in Fig. 6, the TALD composite exhibited a less wavy line compared to the PEALD Al_2O_3/ZnO composites, indicating that TALD produced a smoother surface than PEALD coating on pristine Al_2O_3 IO.

A similar trend was observed for Al_2O_3/TiO_2 composites. TALD composite resulted in a smoother surface (18 nm RMS) compared to PEALD composite (20 nm RMS). The PEALD composite in Fig. 4 displayed a more jagged line, signifying a rougher surface compared to the TALD composite fabricated using TiO_2 infiltration PEALD. These

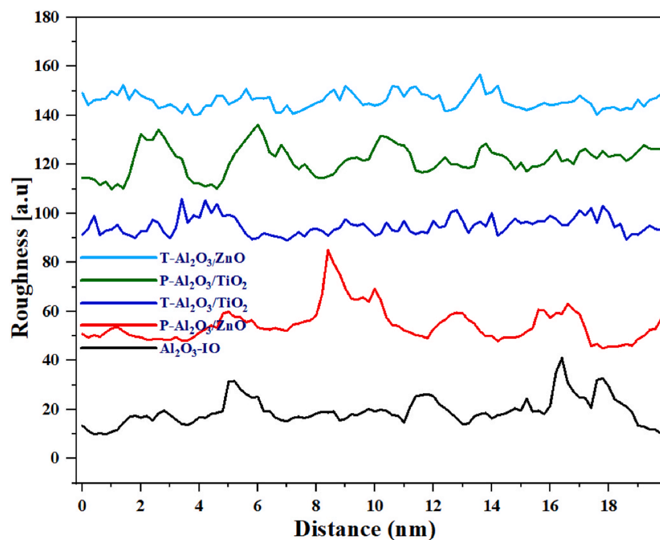

Fig. 5. Roughness of the materials by AFM.

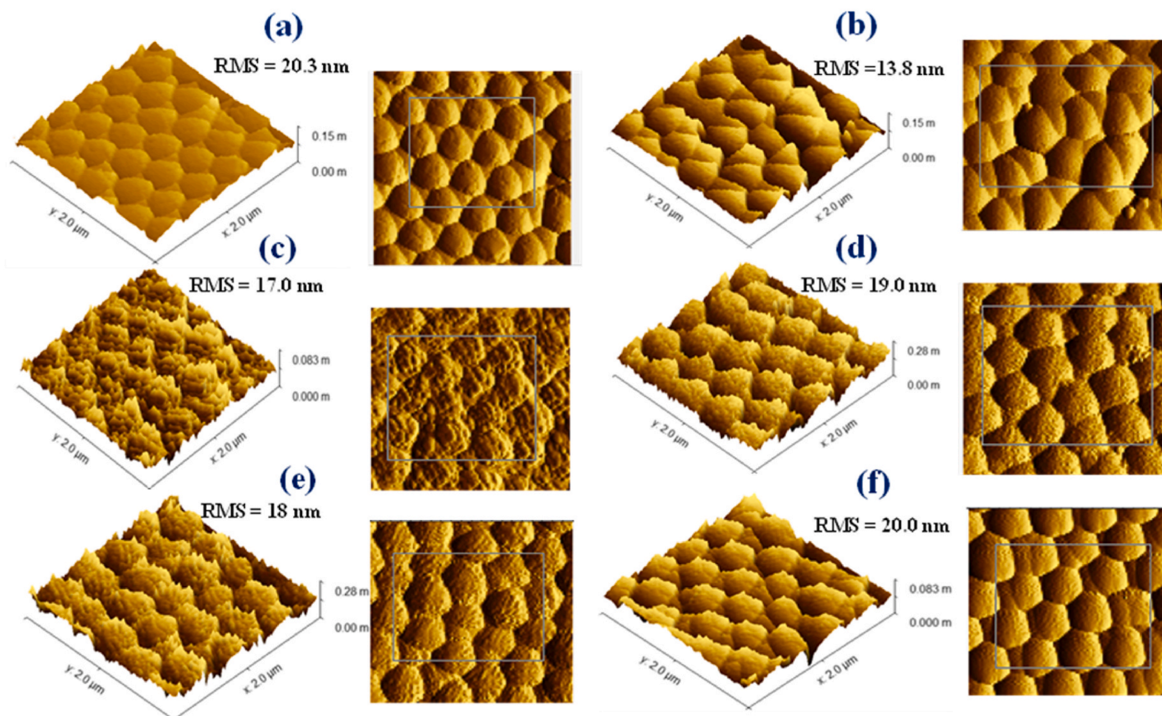

Fig. 4. AFM images of the ALD grown samples: (a) 460-PS nanosphere template, (b) Pristine Al_2O_3 IO, (c) Al_2O_3/ZnO-T, (d) Al_2O_3/ZnO-P, (e) Al_2O_3/TiO_2-T, (f) Al_2O_3/TiO_2-P, respectively.

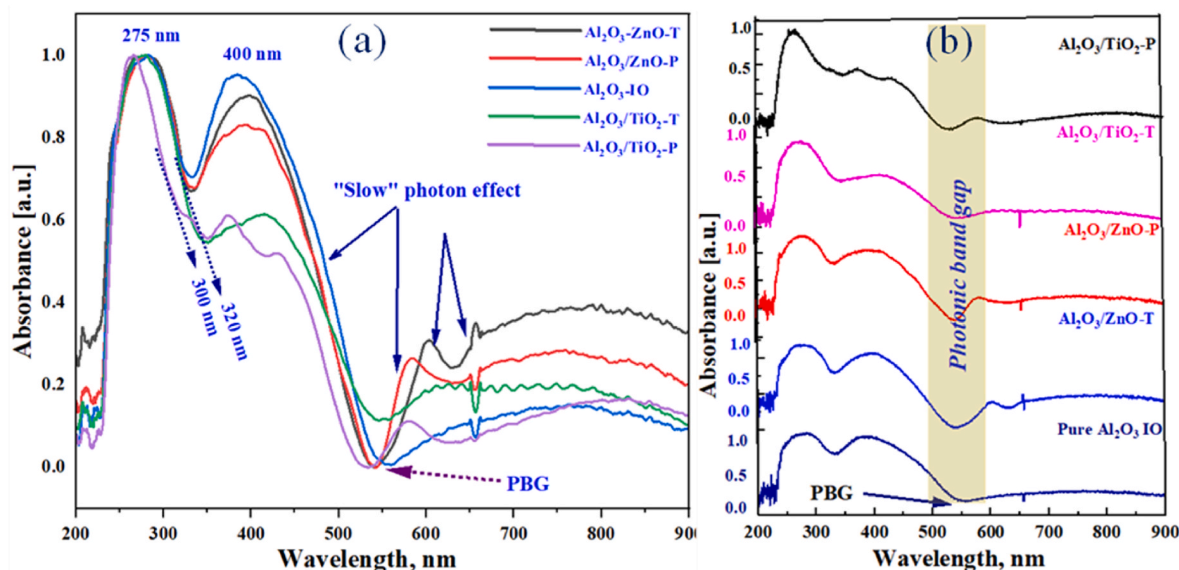

Fig. 6. (a and b) UV Visible absorption spectroscopy of the Al_2O_3 IO and its composite materials.

findings emphasize the significant influence of both the deposition method and the incorporated material on the surface roughness of the IO composites. Notably, TALD generally resulted in smoother surfaces compared to plasma ALD for both ZnO and TiO_2 deposition.

3.5. Optical properties determined by UV Vis spectroscopy

Fig. 7a and b, along with Figure S2 a and b, present the ultraviolet–visible (UV–Vis) absorption, reflectance, and transmittance spectroscopy data for Al_2O_3 IO structures and their composite ALD samples. The pure Al_2O_3 IO and composite samples (with 5 nm ZnO or TiO_2 coated overlayers) have a UV absorption peak at 275 nm, corresponding to the band gap of bulk Al_2O_3 nanoparticles. This is because the UV absorption of Al_2O_3 is determined by its band gap, which is the same for bulk and nanoparticle Al_2O_3 [28]. The absorption edges of all four materials are at 320 nm (Fig. 6a), except for the TiO_2-coated IO PEALD composite, which has an absorption edge of 300 nm. This anomaly is attributed to a combination of factors, including the presence of defects introduced into the TiO_2 layer by the PEALD process, as well as potential changes in stoichiometry or structural variations that could influence the material's electronic properties and shift the absorption edge [29].

Pure Al_2O_3 IO exhibits a prominent additional absorption peak at approximately 400 nm (Fig. 6a). This peak corresponds to enhanced "slow photon" absorption at the short-wavelength (blue) and long-wavelength (red) edges of the PBG centered at 529 nm (Fig. 6 a&b). This implies that pure IO can absorb photons with wavelengths around 400 nm, even though these wavelengths lie outside the PBG. This phenomenon is attributed to the "slow photon" effect, which lengthens the interaction time between light and the IO material, potentially leading to improved efficiency in optoelectronic applications. However, the PBG calculated using Bragg's equation (479 nm, Table 3) is slightly lower than the experimentally determined value (529 nm). This difference can be attributed to several factors. The high-temperature annealing process (900 °C) employed for template removal likely induced shrinkage of the spheres and potentially introduced defects or cracks within the structure. These morphological and structural imperfections are not explicitly considered in the idealized model of Bragg's equation, leading to a deviation from the experimentally observed PBG [30–32].

The UV Visible spectra of both Al_2O_3/ZnO and Al_2O_3/TiO_2 composites (prepared by TALD and PEALD) closely resemble the reference Al_2O_3 (Fig. 6a and b), indicating the minimal influence of the 5 nm ALD coating on the optical properties of the pure material. Consequently, both composite types exhibit a primary PBG around 529 nm (Fig. 7a), consistent with the expected behavior for such thin ZnO and TiO_2 layers. While bulk ZnO nanoparticles possess a narrower band gap (around 373 nm) than Al_2O_3, the calculated PBG values for the composites (482–501 nm) deviate slightly from the experimental 529 nm (Table 3). This discrepancy likely arises from high-temperature annealing shrinking the spheres and disrupting their structural periodicity, a critical factor for PBG.

3.6. Photoluminescence (PL) spectroscopy

Fig. 8 displays the PL results of Al_2O_3, and its composites synthesized through atomic ALD techniques. The improvement in PL intensity of Al_2O_3 IO upon TALD and PEALD coatings can be attributed to enhanced passivation of defect states and modification of optical properties. Fig. 7a illustrates that the pure Al_2O_3 IO exhibits multiple visible light emission peaks at 389, 467, 542, 564, 624, 658, and 674 nm. These peaks span the visible spectrum (approximately 400–750 nm) and correspond to blue, green, and red emissions. The emissions arise from intrinsic defect states in the Al_2O_3 structure, with oxygen vacancies being the primary contributors. Specifically, blue emission peaks (e.g., at 389 nm and 467 nm) are linked to F^+ centers, which are oxygen vacancies with one trapped electron. Green and red emissions (e.g., at 542 nm and 624 nm) are attributed to F^{2+}centers or complex defect configurations involving oxygen vacancies and charge transfer transitions. These attributions align with prior studies that relate specific defect states in Al_2O_3 to visible light PL emissions [33,34].

Similar to pure Al_2O_3 IO, composites, 5 nm ZnO and TiO_2-coated Al_2O_3 IO (Al_2O_3/ZnO-T and Al_2O_3/TiO_2-T) exhibit multiple visible light emission peaks. However, the uncoated Al_2O_3 IO shows the lowest PL intensity (Fig. 7b), likely due to significant non-radiative recombination caused by unpassivated surface defects [35]. When coated with 5 nm ZnO or TiO_2 using TALD or PEALD, the PL intensity of Al_2O_3 IO increases significantly. The ultra-thin ALD coatings improve the bare IO's PL behavior by passivating oxygen vacancies and surface defects, thus reducing non-radiative recombination pathways and enhancing radiative recombination. Among the coated samples, composites with TiO_2 (thermal and plasma ALD) exhibit higher PL intensities than those with ZnO. This suggests that TiO_2 coatings are more effective in passivating defects and enhancing light-matter interactions, possibly due to TiO_2's higher refractive index and stronger optical confinement [36].

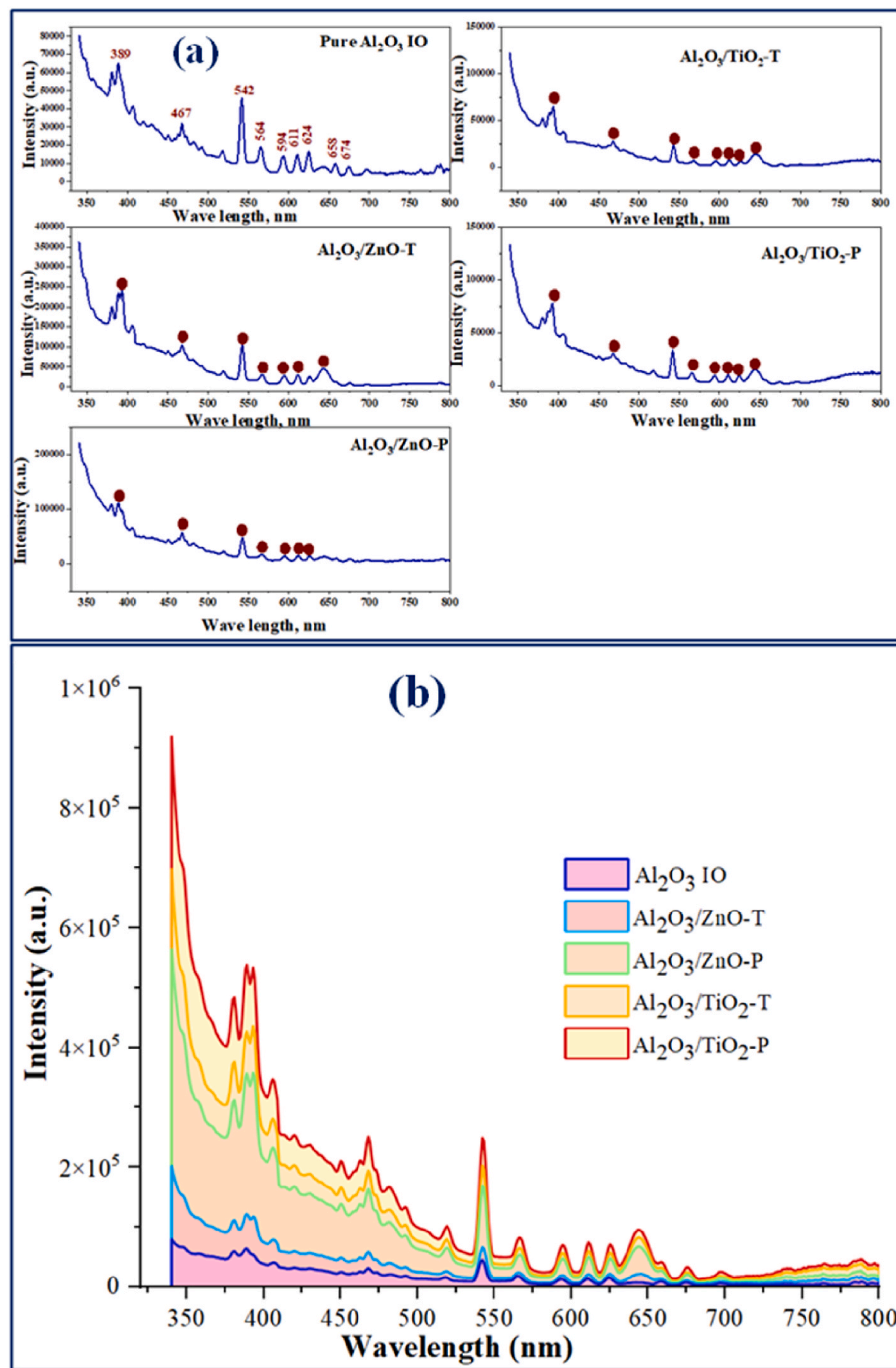

Fig. 7. (a and b) PL emission spectra of the Al_2O_3 IO and its TALD/PEALD composites from ZnO and TiO_2.

Table 3
Summary of PBG properties IO ALD Samples.

Sample	D (nm)	f	% Shrinkage	n_{avg}	PBG position (nm) Calculated	PBG position (nm) Experimental
PS-template	460	0.74	–	1.44	782	–
Pure Al_2O_3 IO	433	0.26	5.9	1.15	479	529
Al_2O_3/ZnO-T	429	0.26	6.7	1.16	482	529
Al_2O_3/ZnO-P	415	0.26	9.8	1.16	482	529
Al_2O_3/TiO_2-T	429	0.26	6.7	1.18	501	529
Al_2O_3/TiO_2-P	415	0.26	9.8	1.18	501	529

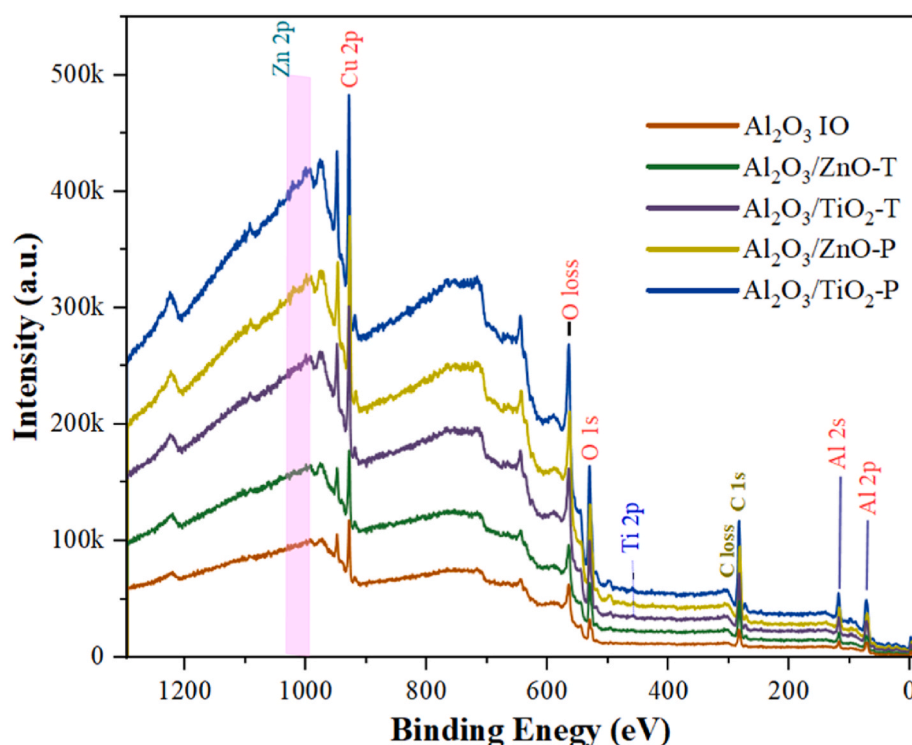

Fig. 8. The XPS measurement results of Al_2O_3 IO and its composite samples.

Additionally, PEALD coatings outperform TALD coatings, as evidenced by the higher PL intensity of PEALD-treated samples. This is likely due to the enhanced reactivity of the plasma species in PEALD, which leads to more effective defect passivation and a uniform, high-quality thin film [37].

However, the narrow PL peaks in ZnO-coated Al_2O_3 IO (Al_2O_3/ZnO-T and Al_2O_3/ZnO-P), despite ZnO's typical broad-band emission [38], indicate that the luminescence predominantly arises from the Al_2O_3 IO structure. This occurs because the ultra-thin ZnO coating (5 nm) lacks sufficient defect density for broad-band emission and acts as a passivating layer, reducing non-radiative recombination and allowing Al_2O_3 defect-related narrow peaks to dominate.

The variation in PL intensity across different wavelengths indicates a complex interplay between the Al_2O_3 IO structure and the deposited layers. The density and type of defect states, as well as the optical properties of the coatings, play a critical role. Overall, both TALD and PEALD improve the PL emission of Al_2O_3 IO, but PEALD coatings demonstrate superior performance due to their plasma-driven reactivity, which enhances the passivation of defects and the uniformity of the coating. TiO_2 coatings are particularly effective, further emphasizing the importance of the deposition method and coating material in modulating the optical properties of Al_2O_3 IO [18,39].

Table 4
The composition of the Al_2O_3 IO and composite samples.

Sample	C	O	Al	Ti	Zn
	%	%	%	%	%
Al_2O_3 IO	54.0	27.0	19.0	–	–
Al_2O_3/ZnO-T	65.4	23.4	10.9	–	0.3
Al_2O_3/TiO_2-T	54.2	27.9	17.3	0.6	–
Al_2O_3/ZnO-P	53.8	26.1	19.0	–	1.1
Al_2O_3/TiO_2-P	51.1	28.1	20.4	0.4	–

3.7. *XPS result*

Fig. 8 and Table 4 present XPS results confirming the successful synthesis and composition of IO structures based on Al_2O_3 and its composites. Fig. 8 reveals characteristic peaks for Al 2p, Al 2s, O 1s, Ti 2p, and Zn 2p, confirming the presence of Al_2O_3 and the successful incorporation of ZnO and TiO_2. A distinct “O loss” peak suggests oxygen vacancies, a common observation in XPS analyses of oxide materials. Additionally, the spectrum hints at the formation of aluminum hydroxide due to hydration, a typical behavior of Al_2O_3 in humid conditions [40]. However, the oxide layers remain stable, with no evidence of carbonate formation. Table 4 further supports these findings, providing elemental composition details. The O content in pure Al_2O_3 IO is approximately 27 %, and Al is 19 %, consistent with the stoichiometric ratio. The high carbon content (50–65 %) across all samples is attributed to surface contamination from atmospheric species and residual ALD precursors.

For Al_2O_3/ZnO composites, the data shows successful ZnO incorporation, with the Al_2O_3/ZnO-T sample containing 0.26 % Zn and the Al_2O_3/ZnO-P sample containing 1.07 % Zn. This suggests that the PEALD is more effective at coating the ZnO layer than the TALD. The oxygen and aluminum percentages remain similar to pure Al_2O_3, indicating that ZnO addition does not significantly alter the overall composition. Whereas, the Al_2O_3/TiO_2 composites show similar trends, with Ti incorporated at 0.6 % in the Al_2O_3/TiO_2-T sample and 0.4 % in the Al_2O_3/TiO_2-P sample. The slight variation between the T and P methods may reflect differences in deposition efficiency or TiO_2 integration within the alumina matrix.

4. Conclusion

In conclusion, this study fabricated IO macrostructures and their composites using polystyrene nanosphere self-assembly ALD techniques. TALD and PEALD were explored for Al_2O_3 infiltration and deposition of ultra-thin composite overlayers (ZnO or TiO_2) within the IO structures. The high-temperature annealing process successfully removed the

sacrificial template, resulting in the final IO structure. However, this process also caused some cracks and shrinkage in the material. The investigation revealed that both deposition methods and incorporated materials influenced the final properties of the IO composites. While TALD generally resulted in smoother surfaces and better conformality compared to PEALD, the introduction of ZnO or TiO_2 layers using either method increased the surface roughness of the IO structures. While both TALD and PEALD composites exhibited a primary PBG around 529 nm, additional PBGs were observed for ZnO and TiO_2 composites due to their respective band gaps. PL analyses revealed that the incorporation of ZnO and TiO_2 layers improved the defect passivation and light-matter interactions of the IO structures. The enhanced PL intensity observed in PEALD-treated samples further confirmed the efficacy of plasma activation in promoting defect passivation and film quality. XPS confirmed successful Al_2O_3, ZnO, and TiO_2 incorporation in IO structures, revealing surface chemistry details like hydroxylation and oxygen vacancies. PEALD showed higher ZnO deposition efficiency than TALD. XPS elucidated surface chemistry and composition, highlighting ALD method influences. Overall, this study establishes a comprehensive framework for the design and optimization of IO structures and their composites using ALD techniques. The findings underscore the versatility of TALD and PEALD in engineering material properties, paving the way for advancements in photonic, catalytic, and optoelectronic applications. Future work could explore the scalability of this approach and the integration of other functional materials to broaden the scope of potential applications.

CRediT authorship contribution statement

Hamsasew Hankebo Lemago: Writing – review & editing, Writing – original draft, Software, Methodology, Investigation, Formal analysis, Data curation, Conceptualization. **Soeun Choi Arwen:** Methodology, Formal analysis, Data curation, Conceptualization. **Dóra Hessz:** Methodology, Investigation, Formal analysis, Data curation, Conceptualization. **Gyula Jágerszki:** Investigation, Funding acquisition, Formal analysis, Data curation, Conceptualization. **Petra Pál:** Methodology, Investigation, Funding acquisition, Formal analysis, Data curation, Conceptualization. **Csaba Cserháti:** Resources, Investigation, Funding acquisition, Formal analysis, Data curation, Conceptualization. **Eszter Mónika Baradács:** Resources, Investigation, Formal analysis, Data curation, Conceptualization. **Tamás Fodor:** Investigation, Funding acquisition, Formal analysis, Data curation, Conceptualization.**Zoltán Erdélyi:** Writing – review & editing, Supervision, Resources, Methodology, Investigation, Funding acquisition, Formal analysis, Data curation, Conceptualization. **Imre Miklós Szilágyi:** Writing – review & editing, Writing – original draft, Supervision, Software, Resources, Methodology, Investigation, Funding acquisition, Formal analysis, Data curation, Conceptualization.

Declaration of competing interest

The authors have no financial relationships with any companies whose products or services are mentioned in this article. The authors have no patents, trademarks, licensed technologies, or copyrights that could be affected by the publication of this article. The authors have no personal relationships with any individuals whose interests could be affected by the publication of this article.

Acknowledgments

The research conducted at BME and reported in this paper was supported by the NRDI Fund (TKP2021 BME-NVA), which was granted by the NRDI Office under the Ministry for Innovation and Technology. Additionally, project no. TKP2021-NKTA-34 was implemented with the support of the Hungarian National Research, Development, and Innovation Fund (NKFIH) under the grant scheme OTKA K143724 and the TKP2021-NKTA funding scheme. The study was further supported by Stipendium Hungaricum, Hungarian government scholarship. The authors would like to express their gratitude to Budapest University of Technology and Economics, the University of Debrecen, and the Tempus Public Foundation for providing valuable online resources, comprehensive databases, and laboratory facilities.

Appendix A. Supplementary data

Supplementary data to this article can be found online at https://doi.org/10.1016/j.vacuum.2025.114254.

Data availability

Data will be made available on request.

References

[1] F. Fathi, M.R. Rashidi, P.S. Pakchin, S. Ahmadi-Kandjani, A. Nikniazi, Photonic crystal based biosensors: emerging inverse opals for biomarker detection, Talanta 221 (2021) 121615, https://doi.org/10.1016/j.talanta.2020.121615.
[2] Y.S. Zhang, C. Zhu, Y. Xia, Inverse opal scaffolds and their biomedical applications, Adv. Mater. 29 (2017) 1–25, https://doi.org/10.1002/adma.201701115.
[3] F. Fathi, H. Monirinasab, F. Ranjbary, K. Nejati-Koshki, Inverse opal photonic crystals: recent advances in fabrication methods and biological applications, J. Drug Deliv. Sci. Technol. 72 (2022) 103377, https://doi.org/10.1016/j.jddst.2022.103377.
[4] R.C. Schroden, M. Al-Daous, C.F. Blanford, A. Stein, Optical properties of inverse opal photonic crystals, Chem. Mater. 14 (2002) 3305–3315, https://doi.org/10.1021/cm020100z.
[5] G. von Freymann, V. Kitaev, B.V. Lotsch, G.A. Ozin, Bottom-up assembly of photonic crystals, Chem. Soc. Rev. 42 (2013) 2528–2554, https://doi.org/10.1039/c2cs35309a.
[6] J.S. King, E. Graugnard, C.J. Summers, TiO2 inverse opals fabricated using low-temperature atomic layer deposition, Adv. Mater. 17 (2005) 1010–1013, https://doi.org/10.1002/adma.200400648.
[7] E. Armstrong, C. O'Dwyer, Artificial opal photonic crystals and inverse opal structures-fundamentals and applications from optics to energy storage, J. Mater. Chem. C 3 (2015) 6109–6143, https://doi.org/10.1039/c5tc01083g.
[8] R.P. Chaukulkar, S. Agarwal, Atomic layer deposition of titanium dioxide using titanium tetrachloride and titanium tetraisopropoxide as precursors, J. Vac. Sci. Technol., A. 31 (2013) 2–7, https://doi.org/10.1116/1.4798385.
[9] Y.-H. Lin, P.-S. Lee, Y.-C. Hsueh, K.-Y. Pan, C.-C. Kei, M.-H. Chan, J.-M. Wu, T.-P. Perng, H.C. Shih, Atomic layer deposition of zinc oxide on multiwalled carbon nanotubes for UV photodetector applications, J. Electrochem. Soc. 158 (2011) K24, https://doi.org/10.1149/1.3522764.
[10] R.W. Johnson, A. Hultqvist, S.F. Bent, A brief review of atomic layer deposition: from fundamentals to applications, Mater. Today 17 (2014) 236–246, https://doi.org/10.1016/j.mattod.2014.04.026.
[11] R.L. Puurunen, Surface chemistry of atomic layer deposition: a case study for the trimethylaluminum/water process, J. Appl. Phys. 97 (2005), https://doi.org/10.1063/1.1940727.
[12] I. Iatsunskyi, M. Kempiński, M. Jancelewicz, K. Załęski, S. Jurga, V. Smyntyna, Structural and XPS characterization of ALD Al2O3 coated porous silicon, Vacuum 113 (2015) 52–58, https://doi.org/10.1016/j.vacuum.2014.12.015.
[13] W. Chiappim, G.E. Testoni, R.S. Moraes, R.S. Pessoa, J.C. Sagás, F.D. Origo, L. Vieira, H.S. MacIel, Structural, morphological, and optical properties of TiO2 thin films grown by atomic layer deposition on fluorine doped tin oxide conductive glass, Vacuum 123 (2016) 91–102, https://doi.org/10.1016/j.vacuum.2015.10.019.
[14] R. Lo Nigro, E. Schilirò, G. Mannino, S. Di Franco, F. Roccaforte, Comparison between thermal and plasma enhanced atomic layer deposition processes for the growth of HfO2 dielectric layers, J. Cryst. Growth 539 (2020) 125624, https://doi.org/10.1016/j.jcrysgro.2020.125624.
[15] H.B. Profijt, S.E. Potts, M.C.M. van de Sanden, W.M.M. Kessels, Plasma-assisted atomic layer deposition: basics, opportunities, and challenges, J. Vac. Sci. Technol., A. 29 (2011), https://doi.org/10.1116/1.3609974.
[16] J.L. van Hemmen, S.B.S. Heil, J.H. Klootwijk, F. Roozeboom, C.J. Hodson, M.C. M. van de Sanden, W.M.M. Kessels, Plasma and thermal ALD of Al[sub 2]O[sub 3] in a commercial 200 mm ALD reactor, J. Electrochem. Soc. 154 (2007) G165, https://doi.org/10.1149/1.2737629.
[17] H.H. Lemago, F.S. Addin, K. Atilla, B. Parditka, D. Hessz, I. Mikl, Synthesis of TiO 2/Al 2 O 3 Double-Layer Inverse Opal by Thermal and Plasma-Assisted Atomic Layer Deposition for Photocatalytic Applications, 2023.
[18] H. Lemago, N. Khauli, D. Hessz, T. Igricz, P. Petra, Fabrication of ZnO-Al 2 O 3 Inverse Opals with Atomic Layer Deposited Amorphous - Al 2 O 3 for Enhanced Photocatalysis, vol. 183, 2024, pp. 1–33, https://doi.org/10.1016/j.mssp.2024.108733.
[19] H.H. Lemago, L. Tolezani, T. Igricz, D. Hessz, P. Pál, C. Cserháti, G. Vecsei, B. Sárközi, E.M. Baradács, Z. Erdélyi, I.M. Szilágyi, Enhanced photocatalysis via inverse opal structures: synthesis and characterization of TiO2/ZnO and ZnO/TiO2

composites using plasma-enhanced ALD, Ceram. Int. (2024), https://doi.org/10.1016/j.ceramint.2024.10.465.
[20] J. Long, M. Fu, C. Li, C. Sun, D. He, Y. Wang, High-quality ZnO inverse opals and related heterostructures as photocatalysts produced by atomic layer deposition, Appl. Surf. Sci. 454 (2018) 112–120, https://doi.org/10.1016/j.apsusc.2018.05.160.
[21] G. Greczynski, L. Hultman, Binding energy referencing in X-ray photoelectron spectroscopy, Nat. Rev. Mater. 10 (2024), https://doi.org/10.1038/s41578-024-00743-5.
[22] M.R. Shamshiri, A.A. Yousefi, M. Pishvaei, F. Ameri, Artificial latex-based opals prepared by spin casting of monodispersed nano particles, J. Polym. Res. 19 (2012), https://doi.org/10.1007/s10965-012-9912-7.
[23] A. Lonergan, D. McNulty, C. O'Dwyer, Tetrahedral framework of inverse opal photonic crystals defines the optical response and photonic band gap, J. Appl. Phys. 124 (2018), https://doi.org/10.1063/1.5033367.
[24] D.R. Boris, V.D. Wheeler, N. Nepal, S.B. Qadri, S.G. Walton, C. Chip, R. Eddy, The role of plasma in plasma-enhanced atomic layer deposition of crystalline films, J. Vac. Sci. Technol., A. 38 (2020), https://doi.org/10.1116/6.0000145.
[25] J.M. Park, S.J. Jang, L.L. Yusup, W.J. Lee, S.I. Lee, Plasma-enhanced atomic layer deposition of silicon nitride using a novel silylamine precursor, ACS Appl. Mater. Interfaces 8 (2016) 20865–20871, https://doi.org/10.1021/acsami.6b06175.
[26] J. Chen, K. Xu, Applications of atomic force microscopy in materials, semiconductors, polymers, and medicine: a minireview, Instrum. Sci. Technol. 48 (2020) 667–681, https://doi.org/10.1080/10739149.2020.1764030.
[27] G.I.N. Waterhouse, M.R. Waterland, Opal and inverse opal photonic crystals: fabrication and characterization, Polyhedron 26 (2007) 356–368, https://doi.org/10.1016/j.poly.2006.06.024.
[28] Z. Gholizadeh, M. Aliannezhadi, M. Ghominejad, F.S. Tehrani, High specific surface area γ-Al2O3 nanoparticles synthesized by facile and low-cost co-precipitation method, Sci. Rep. 13 (2023) 1–14, https://doi.org/10.1038/s41598-023-33266-0.
[29] P. Paul, M.G. Hafiz, P. Schmitt, C. Patzig, F. Otto, T. Fritz, A. Tünnermann, A. Szeghalmi, Optical bandgap control in Al2O3/TiO2 heterostructures by plasma enhanced atomic layer deposition: toward quantizing structures and tailored binary oxides, Spectrochim. Acta Part A Mol. Biomol. Spectrosc. 252 (2021) 119508, https://doi.org/10.1016/j.saa.2021.119508.
[30] Z. Wang, J. Lin, Opal and inverse opal photonic crystals, Chem. Bull./Huaxue Tongbao 67 (2004) 876–882.
[31] E. Armstrong, C. O'Dwyer, Artificial opal photonic crystals and inverse opal structures-fundamentals and applications from optics to energy storage, J. Mater. Chem. C 3 (2015) 6109–6143, https://doi.org/10.1039/c5tc01083g.
[32] T. Baba, Slow light in photonic crystals, Nat. Photonics 2 (2008) 465–473, https://doi.org/10.1038/nphoton.2008.146.
[33] A.I. Kostyukov, A.V. Zhuzhgov, V.V. Kaichev, A.A. Rastorguev, V.N. Snytnikov, V. N. Snytnikov, Photoluminescence of oxygen vacancies in nanostructured Al2O3, Opt. Mater. (Amst). 75 (2018) 757–763, https://doi.org/10.1016/j.optmat.2017.11.040.
[34] D. Gupta, V. Chauhan, N. Koratkar, F. Singh, A. Kumar, S. Kumar, R. Kumar, High energy (MeV) ion beam induced modifications in Al2O3-ZnO multilayers thin films grown by ALD and enhancement in photoluminescence, optical and structural properties, Vacuum 192 (2021), https://doi.org/10.1016/j.vacuum.2021.110435.
[35] V.A. Pustovarov, T.V. Perevalov, V.A. Gritsenko, T.P. Smirnova, A.P. Yelisseyev, Oxygen vacancy in Al2O3: photoluminescence study and first-principle simulation, Thin Solid Films 519 (2011) 6319–6322, https://doi.org/10.1016/j.tsf.2011.04.014.
[36] L.D.V. Sangani, M.A. Mohiddon, G. Rajaram, M.G. Krishna, Optical confinement in TiO2 waveguides fabricated by resist free electron beam lithography, Opt. Laser Technol. 123 (2020), https://doi.org/10.1016/j.optlastec.2019.105901.
[37] M. Peng, X. Zheng, S. Liu, H. Wei, Y. He, M. Li, Y. An, Y. Song, P. Qiu, A. large-scale, ultrahigh-resolution nanoemitter ordered array with PL brightness enhanced by PEALD-grown AlN coating, Nanoscale 11 (2019) 3710–3717, https://doi.org/10.1039/c8nr07946c.
[38] A. Singh, A. Mathur, D. Pal, A. Sengupta, R. Singh, S. Chattopadhyay, Near room temperature atomic layer deposition of ZnO thin films on poly (methyl methacrylate) (PMMA) templates: a study of structure, morphology and photoluminescence of ZnO as an effect of template confinement, Vacuum 161 (2019) 398–403, https://doi.org/10.1016/j.vacuum.2019.01.006.
[39] Y. Jin, M. Govoni, G. Wolfowicz, S.E. Sullivan, F.J. Heremans, D.D. Awschalom, G. Galli, Photoluminescence spectra of point defects in semiconductors: validation of first-principles calculations, Phys. Rev. Mater. 5 (2021), https://doi.org/10.1103/PhysRevMaterials.5.084603.
[40] P. Jin, G. Xu, M. Tazawa, K. Yoshimura, D. Music, J. Alami, U. Helmersson, O. Al, P. Jin, G. Xu, M. Tazawa, K. Yoshimura, Low Temperature Deposition of α- Al 2 O 3 Thin Films by Sputtering Using a Cr 2 O 3 Template Low Temperature Deposition of _ -Al 2 O 3 Thin Films by Sputtering Using a Cr 2 O 3 Template, vol. 2134, 2007, pp. 10–13.